

Magnetic mesh generation and field line reconstruction for scrape-off layer and divertor modeling in stellarators

H. Frerichs¹, D. Boeyaert¹, Y. Feng², K.A. Garcia¹

¹ Department of Nuclear Engineering & Engineering Physics, University of Wisconsin - Madison, WI, USA

² Max-Planck-Institut für Plasmaphysik, Greifswald, Germany

E-mail: hfrerichs@wisc.edu

Abstract. The design of divertor targets and baffles for optimal heat and particle exhaust from magnetically confined fusion plasmas requires a combination of fast, low-fidelity models (such as EMC3-lite [1]) for scoping studies and high-fidelity ones (such as EMC3-EIRENE [2]) for verification. Both of those approaches benefit from a magnetic flux tube mesh for fast interpolation and mapping of field line segments [3]. A new mesh generator for unstructured quadrilateral flux tubes with adaptive refinement is presented and integrated into FLARE [4]. For HSX with an extended first wall, it is found that several layers of flux tubes can span the entire half field period before splitting is required. This is an advantage over the traditional setup of the EMC3-EIRENE mesh where careful construction of several sub-domains is required already for the much tighter present first wall. The divide and conquer paradigm with unstructured mesh layout offers a powerful alternative for integration into optimization workflows. Further examples for W7-X and CTH are presented.

Keywords: mesh generation, magnetic field lines, scrape-off layer & divertor plasma modeling

1. Introduction

The stellarator path towards magnetic confinement fusion power offers great design flexibility (e.g. number of field periods, modular vs. helical coils, quasi-symmetric vs. quasi-isodynamic configurations ...) for leveraging its advantage of improved stability and intrinsic steady-state operation compared to tokamaks [5, 6]. A common challenge for both concepts is the control of particle and heat exhaust from the scrape-off layer (SOL) at acceptable levels for plasma material interactions and impurity accumulation [7]. However, the increased complexity of stellarators introduces further difficulties for divertor design such as toroidal localization of heat load peaks and inefficient pumping of neutral particles due to poor closure.

The optimization of divertor targets and baffles requires a combination of fast, low-fidelity models for scoping studies and high-fidelity ones for verification. The EMC3-EIRENE code [8, 9, 2] is currently the workhorse for divertor and scrape-off layer analysis in W7-X [10, 11, 12, 13, 14]. It is based on a fluid model for the steady state plasma (EMC3) which is coupled to a kinetic model for neutrals (EIRENE), and it includes cooling from radiation of intrinsic or seeded impurities. Self-consistent solution of the non-linear equations requires an iterative procedure, and convergence can take a significant number of iterations under detached conditions. Therefore, it is currently not suitable to integrate EMC3-EIRENE into an optimization scheme. However, a linearized reduced model (EMC3-lite [1]) has been developed recently for fast approximation of heat loads supporting the design of the new tungsten divertor at W7-X [15]. Even though EMC3-lite cannot model detachment, it can be used to minimize the heat loads that a divertor needs to handle in the first place.

Both of these approaches benefit from a magnetic flux tube mesh for fast interpolation and mapping of field line segments [3]. Nevertheless, construction of such a mesh often needs manual adjustments in order to avoid gaps in the simulation domain and to ensure that the cross-sections of all flux tubes remain convex in order to support a unique inverse transformation from cylindrical to local coordinates (see cartoon of good vs. bad flux tube in figure 1). The 3D mesh is typically constructed by field line tracing from a (block-)structured 2D base mesh. Gaps can occur where field lines travel radially inwards from plasma exposed surfaces if the base mesh does not extend sufficiently beyond those. On the other hand, proximity to coils and strong magnetic shear can result in flux conservation errors and invalid flux tube cross-sections. Thus, construction of the base mesh often requires fine tuning. A quasi-orthogonal mesh may be favorable for good flux tube shape, but can result in extremely packed or inadequate poloidal spacing.

A new mesh generator for unstructured quadrilateral flux tubes with adaptive refinement is presented in section 2 and integrated into (the development branch of) the FLARE code [4]. First, starting from a pair of good flux surfaces, an initial layer of flux tubes is constructed across the specified toroidal domain (such as the half field period in stellarators). Then, layers of flux tubes are added incrementally while the poloidal resolution can be increased locally as needed. Whenever the new flux tubes fail quality checks, they are discarded and the current toroidal domain is split in half from there on outwards. The entire volume up to the first wall (or any poloidally and toroidally closed magnetic field line casing) is eventually filled with flux tubes. Divertor targets and baffles can be added and modified later within the given casing for heat and particle exhaust optimization studies. Examples for CTH, HSX and W7-X are presented in section 3.

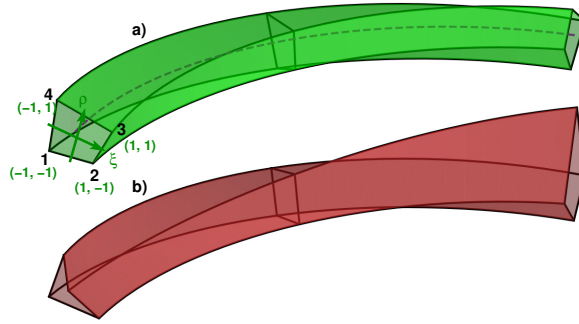


Figure 1. (a) Finite flux tube with local coordinate system (ξ, ρ) and interpolated field line (dashed), (b) flux tube with invalid cross-section on the left side.

2. Adaptive flux tube mesh construction

The common basis for the new mesh generator and the EMC3 standard is a pair of good flux surfaces at the edge of the core region. These flux surfaces can be selected from a Poincaré plot from which a smooth representation can be generated (see e.g. section 3.5.2 in [4]). Typically, the toroidal domain (i.e. half field period in stellarators) is split into toroidal blocks for EMC3, and a base mesh is constructed for each block. While W7-X simulations can get away with a single 36 deg block, the simulation domain for HSX (45 deg) needs to be split into 5 blocks of 9 deg [16] due to deformation of flux tubes from large radial excursions of field lines. Then, the outer boundary for the base mesh in each block needs to be chosen carefully such that no gaps develop in the 3D grid. This can take several manual iterations, and extending the first wall with space for divertor targets and baffles only further complicates mesh construction [17, 18]. In the new approach outlined here, we start with a single base mesh at the center of the domain and work our way outwards. We start with a brief introduction of field line interpolation in section 2.1 before presenting the new algorithm for adaptive flux tube mesh construction in section 2.2.

2.1. Field line interpolation

In toroidal configurations, a magnetic field line is constructed by integrating the system of ordinary differential equations

$$\frac{dr}{d\varphi} = r \frac{B_r}{B_\varphi}, \quad \frac{dz}{d\varphi} = r \frac{B_z}{B_\varphi} \quad (1)$$

from an initial point $\mathbf{p}_i = (r_i, z_i, \varphi_i)$. The right hand side of (1) is given by the local magnetic field vector $\mathbf{B}(\mathbf{p}) = (B_r, B_z, B_\varphi)$ at $\mathbf{p} = (r, z, \varphi)$. See section 3.1 in [4] for a discussion of numerical methods implemented in FLARE. In the following, let $\mathbf{F}(\varphi) = (r(\varphi), z(\varphi))$ be a numerical approximation of such field line over some toroidal domain T . A finite quadrilateral flux tube is then defined by four of such segments

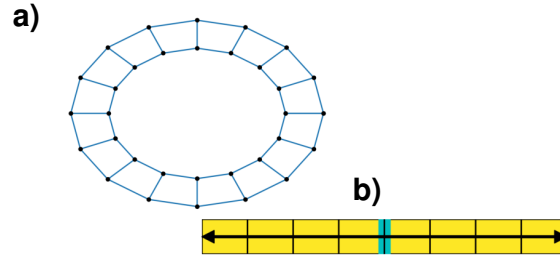


Figure 2. (a) Initial layer of cells constructed from pair of good flux surface contours, (b) flux tube segments are constructed by tracing field lines from the base mesh (cyan) towards either end of the domain.

as shown in figure 1 (a). Within each flux tube, bilinear interpolation is applied to reconstruct a field line segment

$$\mathbf{F}_{\xi\rho}^{(\mathbf{t})}(\varphi) = \sum_{i=1}^4 \mathbf{F}_{it}(\varphi) \frac{1}{4} (1 + \xi_i \xi) (1 + \rho_i \rho), \quad \varphi \in T \quad (2)$$

for given local coordinates $(\xi, \rho) \in [-1, 1]^2$. The coefficients (ξ_i, ρ_i) in (2) are the local coordinates associated with the 4 guiding field lines \mathbf{F}_{it} for flux tube \mathbf{t} . Reconstruction of a field line beyond the domain T is based on a reversible mapping

$$\mathbf{F}_{\xi\rho}^{(\mathbf{t})}(\varphi_{\text{map}}) = \mathbf{F}_{\xi'\rho'}^{(\mathbf{t}')}(\varphi_{\text{map}}) \quad (3)$$

at the interface φ_{map} between flux tube (\mathbf{t}) and an appropriate neighbor (\mathbf{t}') (see e.g. figure 4 in [19]). The cross-section of the flux tube should remain convex throughout T such that the inverse transformation from cylindrical to local coordinates is unique. A counter example is shown in figure 1 (b).

2.2. New algorithm

First, a single layer of cells is constructed from a pair of good flux surface contours at the center of the simulation domain as indicated in figure 2. The poloidal resolution m_p is an input parameter and determines the poloidal reference length Δ_p . Another input is the toroidal discretization $(\varphi_k), k = 0, \dots, n_\varphi$. An initial ring of flux tubes is then generated from field line tracing across the domain $[\varphi_0, \varphi_{n_\varphi}]$. Because it is generated from good flux surfaces, it can be assumed that this initial ring of flux tubes passes the quality check for flux conservation and shape. This is indeed the case for the examples presented later. From here, layers of flux tubes are added incrementally until the entire specified volume is filled with flux tubes. Divertor targets and baffles are not taken into account at this point. Rather, a maximal volume is specified in which divertor target and baffle geometry can be optimized later. This magnetic field line casing should exclude any coils and is required as input.

A new layer of cells is added to the base mesh as indicated in figure 3 (a). For each mesh node \mathbf{x}_{ij} , a new mesh node is placed at

$$\mathbf{x}_{i,j+1} = \mathbf{x}_{ij} + \Delta_r \mathbf{r}_{ij} \quad (4)$$

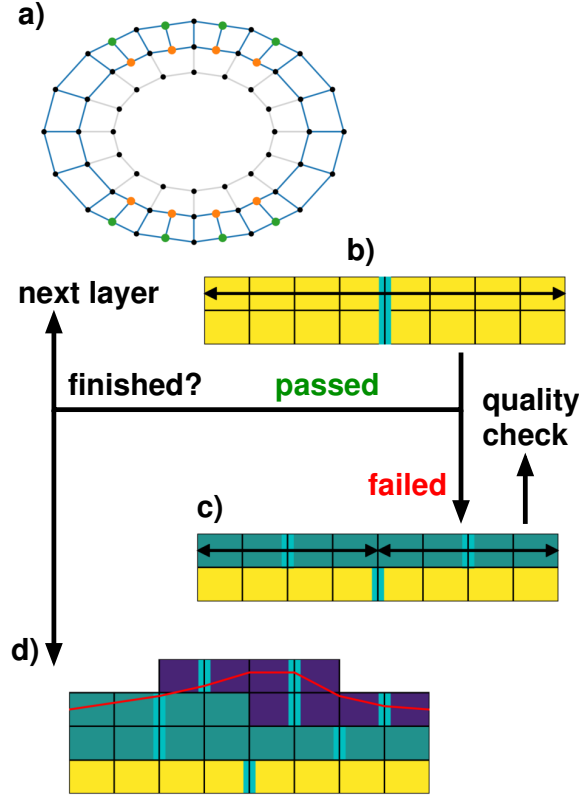


Figure 3. (a) New layer of cells added to base mesh with adaptive poloidal refinement, (b) flux tube segments are constructed by tracing field lines from the new layer of the base mesh (cyan), (c) if quality check fails, the domain is divided and a new base mesh is initialized for each sub-domain for which flux tubes are generated, (d) layers are added incrementally until the entire volume inside a magnetic field line casing (red) is filled.

where \mathbf{r}_{ij} is the unit normal vector associated with the secant $\mathbf{x}_{i+1j} - \mathbf{x}_{i-1j}$. The radial width Δ_r is another input parameter. The poloidal resolution of the new ring is determined by Δ_p : new nodes (highlighted green) are inserted where the new poloidal cell edges exceed $2\Delta_p$, and virtual nodes (highlighted orange) are placed along the old edge. Then, as indicated in figure 3 (b), flux tubes are generated by tracing field lines from the new layer of nodes in the base mesh across the toroidal domain $[\varphi_a, \varphi_b], 0 \leq a < b \leq n_\varphi$. No field lines are traced from virtual nodes. Rather, a virtual field line is defined from the midpoints of two field lines i_1 and i_2 :

$$\mathbf{F}_{(i_1, i_2)}(\varphi) = \frac{1}{2} (\mathbf{F}_{i_1}(\varphi) + \mathbf{F}_{i_2}(\varphi)). \quad (5)$$

The virtual field line is always located along the straight edge between the two guiding field lines such that no gap is introduced along the way. However, this introduces a 1-many neighbor relation for some flux tubes. Finally, the new layer is evaluated and flux tubes that are completely outside the first wall are tagged as unnecessary (and later removed). For the quality check of the remaining flux tubes, cross-sections are

evaluated at $\varphi_k, k = a \dots b$ and the entire layer is discarded if a non-convex cross-section is detected. A future improvement could be to repair a (weakly damaged) flux tube by adjusting the base mesh similar to what is proposed in [20]. Furthermore, the magnetic flux Φ_k through each segment $[\varphi_{k-1}, \varphi_k]$ is computed, and the violation of flux conservation

$$\Delta_{\Phi} = \frac{\max \Phi_k - \min \Phi_k}{\sum_{k=a+1}^b \Phi_k} \quad (6)$$

is compared to the acceptable error $\Delta_{\Phi \max}$ provided as input. If the quality check fails, the current toroidal domain is divided in two and a new base mesh is initialized at the center of each sub-domain as indicated in figure 3 (c). The 3D flux tube mesh is constructed recursively from there on out as shown in figure 3 (d) until the entire volume inside the first wall is filled.

It may be acceptable to allow a few flux tubes with moderate flux conservation error within a layer, in particular if those end up carrying little heat flux. This is implemented by setting a moderate value for $\Delta_{\Phi \max}$ and a lower value for $\Delta_{\Phi \text{avg}}$ provided as additional input parameter. The latter is used as a constrained for the average violation of flux conservation

$$\overline{\Delta}_{\Phi} = \frac{1}{m_p^{\circ}} \sum_{i=1}^{m_p^*} \delta_i \Delta_{\Phi i}, \quad m_p^{\circ} = \sum_{i=1}^{m_p^*} \delta_i \quad (7)$$

where m_p^* is the adapted number of flux tubes (after refinement) within the current layer and $\delta_i = 0, 1$ removes contributions from unnecessary flux tubes. As fewer flux tubes remain towards the first wall, (7) is compared to

$$\Delta_{\Phi \text{avg}}^* = \Delta_{\Phi \max} + (\Delta_{\Phi \text{avg}} - \Delta_{\Phi \max}) \cdot \frac{m_p^{\circ} - 1}{m_p^* - 1} \quad (8)$$

which evaluates to $\Delta_{\Phi \text{avg}}$ for the initial layer and imposes a weaker constraint near the first wall where few flux tubes remain.

3. Examples

The new mesh generator has been applied to configurations at CTH, HSX and W7-X. The first examples shown in the upper row of figure 4 is the 10 kA configuration in CTH with a wide chaotic edge [21]. An artificial first wall is taken at a minor radius of 25 cm instead of the regular 29 cm because some margin is needed for the domain of definition for the magnetic field. The magnetic field is input for FLARE [4] and can be re-computed in a larger domain for future CTH applications. The second example shown in the middle row of figure 4 is the standard quasi-helically symmetric (QHS) configuration in HSX - but with an extended wall that has been recently proposed [18]. The third example shown in the lower row of figure 4 is the standard divertor configuration in W7-X for which only the first wall (red) is used during mesh generation. Mesh parameters are summarized in table 1.

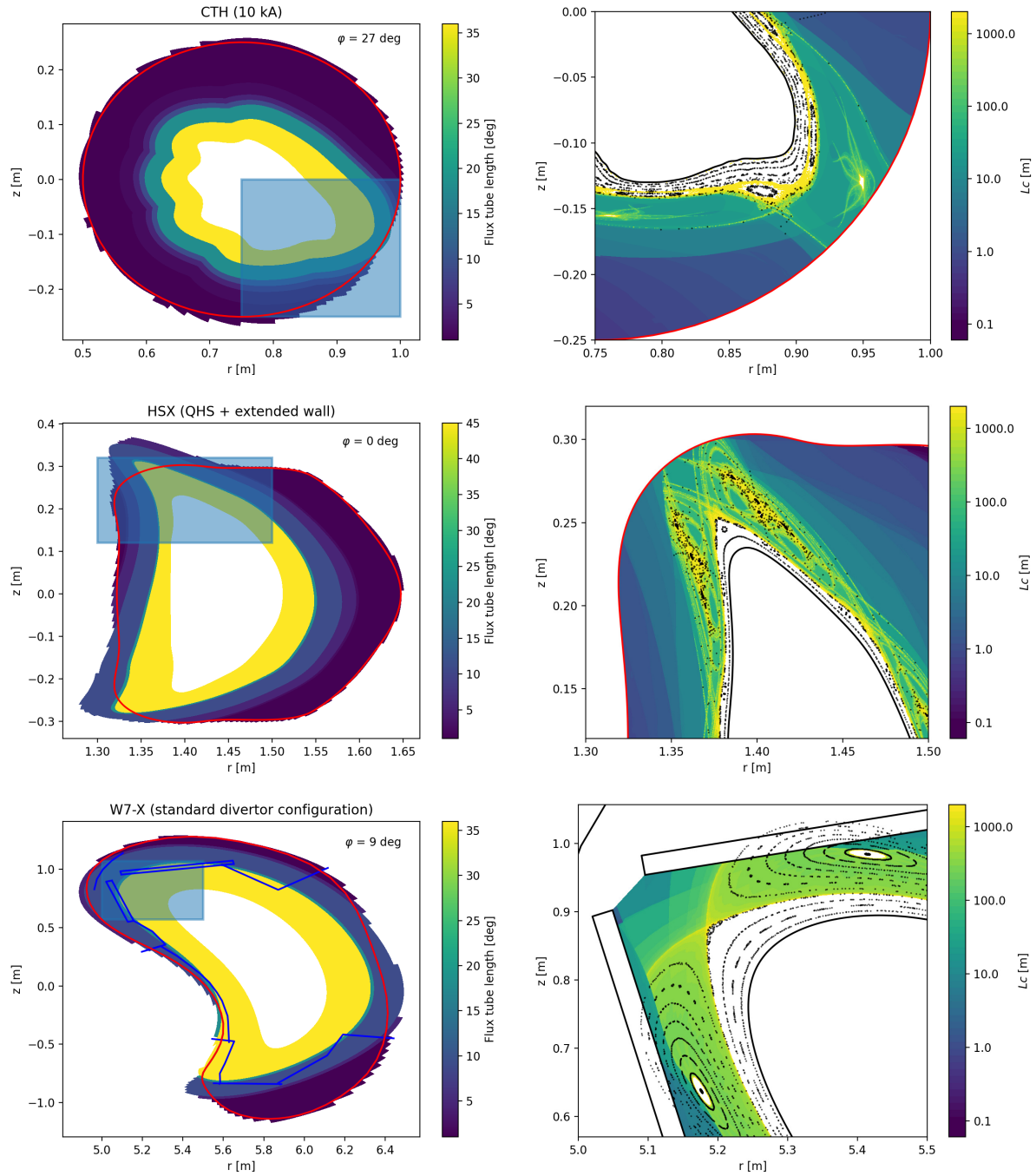


Figure 4. Examples for CTH (upper row), HSX (middle row) and W7-X (lower row): (left) flux tube length within the mesh, (right) connection length and Poincaré plots from field line reconstruction. Divertor targets were not active for the Poincaré plot for W7-X in order to highlight the island structure.

	symmetry	major rad. [m]	minor rad. [m]	m_p	Δ_r [mm]	$\Delta\Phi_{\max}$	$\Delta\Phi_{\text{avg}}$
CTH	5	0.75	0.29	360	2	0.3	0.3
HSX	4	1.2	0.15	360	3	0.3	0.3
W7-X	5	5.5	0.53	360	8	0.45	0.1

Table 1. Geometry and mesh parameters for the three example configurations.

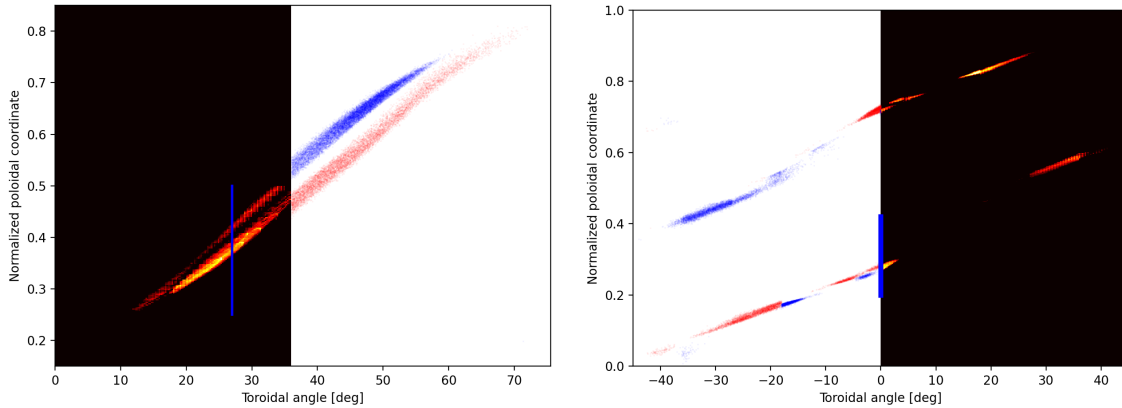


Figure 5. Footprint analysis on the first wall for CTH (left) and HSX (right): strike points from field line tracing with diffusion in forward (red) and backward (blue) direction are shown on white background in one half of the field period, and heat load approximations equivalent to EMC3-lite are shown on black background in the other half of the field period.

It can be seen in the left column of figure 4 that flux tubes can be constructed across the entire simulation domain for several layers (yellow) in all configurations before splitting is required. For HSX, this is an advantage over the traditional setup of the EMC3-EIRENE mesh where careful construction of several sub-domains is required already for the much tighter present first wall. Only far scrape-off layer flux tubes need to be split. In particular, there is no need to find a suitable outer boundary for the base mesh (at several toroidal locations) that is necessary in the traditional setup. High resolution connection length plots can be generated from field line reconstruction as shown in the right column of figure 4, and Poincaré plots are overlaid in black. For W7-X, divertor targets and baffles are added for the connection length computation but were deactive for the Poincaré plots in order to highlight the island structure.

Artificial cross-field diffusion \mathcal{D} during field line tracing can mimic particle or energy transport $D = \mathcal{D}u$ in a fluid at velocity u . Strike points from field line tracing with $\mathcal{D} = 10^{-5} \text{ m}^2 \text{ m}^{-1}$ are shown in figures 5 and 6 as reference. A new heat load approximation module has been developed that follows the EMC3-lite approach based on solving the linearized heat conduction equation [1], and results are shown in figures 5 and 6 for comparison. Here, a diffusivity of $\chi = 1 \text{ m}^2 \text{ s}^{-1}$ is used, and it can be seen

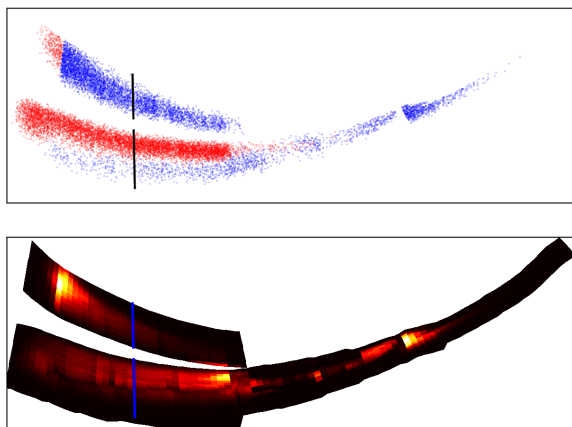


Figure 6. Footprint analysis on the divertor targets in W7-X: strike points from field line tracing with diffusion in forward (red) and backward (blue) direction are shown (upper figure), and heat load approximations equivalent to EMC3-lite are shown on black background (lower figure).

that the heat load maps mirror the striation pattern of field line strike points. This fast approximation of head loads is intended for integration into optimization workflows for divertor target and baffle design.

4. Conclusions

A new mesh generator for unstructured quadrilateral flux tubes with adaptive refinement has been presented as an extension of the FLARE code. It has been found that several layers of flux tubes can span the entire half field period before splitting of flux tubes is required. This is an advantage over the traditional setup of the EMC3-EIRENE mesh where careful construction of several sub-domains is required for configurations like HSX. Furthermore, there is no need to find suitable outer boundary for the base mesh (at several toroidal location). The new adaptive flux tube mesh generator combined with fast head load approximation offers a powerful tool for integration into optimization workflows for divertor target and baffle design. An extension of EMC3-EIRENE for more flexible mesh layouts may be of interest as a future project.

Acknowledgments

This work was supported by the U.S. Department of Energy under awards No. P-240001537 and DE-SC0014210.

References

- [1] Y Feng and W7-X-team. Review of magnetic islands from the divertor perspective and a simplified heat transport model for the island divertor. *Plasma Physics and Controlled Fusion*, **64**

- (2022) (12) 125012. [10.1088/1361-6587/ac9ed9](https://doi.org/10.1088/1361-6587/ac9ed9).
- [2] Y. Feng, H. Frerichs, M. Kobayashi, A. Bader, F. Effenberg, D. Harting, H. Hoelbe, J. Huang, G. Kawamura, J. D. Lore, T. Lunt, D. Reiter, O. Schmitz, and D. Sharma. Recent Improvements in the EMC3-Eirene Code. *Contrib. Plasma Phys.*, **54** (2014) (4-6) 426–431. [10.1002/ctpp.201410092](https://doi.org/10.1002/ctpp.201410092).
- [3] Y. Feng, F. Sardei, and J. Kisslinger. A simple highly accurate field-line mapping technique for three-dimensional Monte Carlo modeling of plasma edge transport. *Phys. Plasmas*, **12** (2005) (052505) 1–7. [10.1063/1.1888959](https://doi.org/10.1063/1.1888959).
- [4] H. Frerichs. FLARE: field line analysis and reconstruction for 3D boundary plasma modeling. *Nuclear Fusion*, **64** (2024) 106034. [10.1088/1741-4326/ad7303](https://doi.org/10.1088/1741-4326/ad7303).
- [5] A. H. Boozer. Stellarator design. *J. Plasma Phys.*, **81** (2015) (06) 515810606. [10.1017/S0022377815001373](https://doi.org/10.1017/S0022377815001373).
- [6] Allen H. Boozer. Needed computations and computational capabilities for stellarators. *Physics of Plasmas*, **31** (2024) (6). ISSN 1089-7674. [10.1063/5.0211063](https://doi.org/10.1063/5.0211063).
- [7] R. König, P. Grigull, K. McCormick, Y. Feng, J. Kisslinger, A. Komori, S. Masuzaki, K. Matsuoka, T. Obiki, N. Ohyabu, H. Renner, F. Sardei, F. Wagner, and A. Werner. The divertor program in stellarators. *Plasma Phys. Control. Fusion*, **44** (2002) (11) 2365–2422.
- [8] Y. Feng, F. Sardei, J. Kisslinger, P. Grigull, K. McCormick, and D. Reiter. 3D Edge Modeling and Island Divertor Physics. *Contrib. Plasma Phys.*, **44** (2004) (1-3) 57–69. [10.1002/ctpp.200410009](https://doi.org/10.1002/ctpp.200410009).
- [9] D. Reiter, M. Baelmans, and P. Boerner. The EIRENE and B2-EIRENE codes. *Fusion Science and Technology*, **47** (2005) (2) 172. [10.13182/FST47-172](https://doi.org/10.13182/FST47-172).
- [10] Y. Feng, C.D. Beidler, J. Geiger, P. Helander, H. Hölbe, H. Maassberg, Y. Turkin, D. Reiter, and W7-X Team. On the W7-X divertor performance under detached conditions. *Nuclear Fusion*, **56** (2016) 126011. [10.1088/0029-5515/56/12/126011](https://doi.org/10.1088/0029-5515/56/12/126011).
- [11] F. Effenberg, S. Brezinsek, Y. Feng, R. König, M. Krychowiak, M. Jakubowski, H. Niemann, V. Perseo, O. Schmitz, D. Zhang, T. Barbui, C. Biedermann, R. Burhenn, B. Buttenschön, G. Kocsis, A. Pavone, F. Reimold, T. Szepesi, H. Frerichs, Y. Gao, U. Hergenhahn, S. Kwak, M. Otte, and T. Sunn Pedersen and. First demonstration of radiative power exhaust with impurity seeding in the island divertor at Wendelstein 7-X. *Nuclear Fusion*, **59** (2019) (10) 106020. [10.1088/1741-4326/ab32c4](https://doi.org/10.1088/1741-4326/ab32c4).
- [12] Y. Feng, M. Jakubowski, R. König, M. Krychowiak, M. Otte, F. Reimold, D. Reiter, O. Schmitz, D. Zhang, C.D. Beidler, C. Biedermann, S. Bozhentkov, K.J. Brunner, A. Dinklage, P. Drewelow, F. Effenberg, M. Endler, G. Fuchert, Y. Gao, J. Geiger, K.C. Hammond, P. Helander, C. Killer, J. Knauer, T. Kremeyer, E. Pasch, L. Rudischhauser, G. Schlisio, T. Sunn Pedersen, U. Wenzel, V. Winters, and W7-X team. Understanding detachment of the w7-x island divertor. *Nuclear Fusion*, **61** (2021) (8) 086012. [10.1088/1741-4326/ac0772](https://doi.org/10.1088/1741-4326/ac0772).
- [13] O. Schmitz, Y. Feng, M. Jakubowski, R. König, M. Krychowiak, M. Otte, F. Reimold, T. Barbui, C. Biedermann, S. Bozhentkov, S. Brezinsek, B. Buttenschön, K.J. Brunner, P. Drewelow, F. Effenberg, E. Flom, H. Frerichs, O. Ford, G. Fuchert, Y. Gao, D. Gradic, O. Grulke, K. C. Hammond, U. Hergenhahn, U. Höfel, J. Knauer, P. Kornejew, T. Kremeyer, H. Niemann, E. Pasch, A. Pavone, V. Perseo, L. Rudischhauser, G. Schlisio, T. Sunn Pedersen, U. Wenzel, V. Winters, G.A. Wurden, D. Zhang, and the W7-X team. Stable heat and particle flux detachment with efficient particle exhaust in the island divertor of Wendelstein 7-X. *Nuclear Fusion*, **61** (2021) 016026. [10.1088/1741-4326/abb51e](https://doi.org/10.1088/1741-4326/abb51e).
- [14] D. Boeyaert, Y. Feng, H. Frerichs, T. Kremeyer, D. Naujoks, Reimold F, O. Schmitz, V. Winters, Bozhentkov S, Fellingner J, V. Perseo, G. Schlisio, U. Wenzel, and W7-X team. Analysis of the neutral flows in the divertor region of Wendelstein 7-X under attached and detached conditions using EMC3-EIRENE. *Plasma Phys. Control. Fusion*, **66** (2024). [10.1088/1361-6587/ad0e22](https://doi.org/10.1088/1361-6587/ad0e22).
- [15] Yu Gao, Yuhe Feng, Michael Endler, Marcin W. Jakubowski, Joachim Geiger, Sergey Bozhentkov, Aleix Puig Sitjes, Fabio Pisano, Chandra Prakash Dhard, Dirk Naujoks, Maciej Krychowiak,

- Matthias Otte, Ralf König, Daihong Zhang, Georg Schlisio, Uwe Wenzel, Thomas Sunn Pedersen, and the W7-X Team. Improvement in the simulation tools for heat distribution predictions and control of baffle and middle divertor loads in wendelstein 7-x. *Nuclear Fusion*, **63** (2023) (2) 026031. [10.1088/1741-4326/acaf0e](https://doi.org/10.1088/1741-4326/acaf0e).
- [16] A. Bader, D. T. Anderson, C. C. Hegna, Y. Feng, J. D. Lore, and J. N. Talmadge. Simulation of edge configurations in quasi-helically symmetric geometry using EMC3-EIRENE. *Nuclear Fusion*, **53** (2013) 113036. [10.1088/0029-5515/53/11/113036](https://doi.org/10.1088/0029-5515/53/11/113036).
- [17] Dieter Boeyaert, Kelly A. Garcia, Heinke Frerichs, Michael J. Gerarda, Aaron Bader, Robert Davies, Benedikt Geiger, John Schmitt, and Oliver Schmitz. Towards improved neutral exhaust in the hsx stellarator. *Nuclear Mater. Energy*, **submitted to** (2024).
- [18] John Schmitt, Dieter Boeyaert, Aaron Bader, Robert Davies, Heinke Frerichs, Kelly Garcia, and Jacob Nesbit. Vacuum vessel design with lofted toroidal surfaces for a qhs configuration. *Fusion Engineering and Design*, **submitted to** (2024).
- [19] H. Frerichs, D. Reiter, Y. Feng, and D. Harting. Block-structured grids in Lagrangian 3D edge plasma transport simulations. *Comp. Phys. Commun.*, **181** (2010) 61–70. [10.1016/j.cpc.2009.08.016](https://doi.org/10.1016/j.cpc.2009.08.016).
- [20] Daisuke TAKADA, Taku ITOH, Masahiro KOBAYASHI, and Hiroaki NAKAMURA. A mesh-generation scheme for the large helical device based on the structure of magnetic-field lines. *Plasma and Fusion Research*, **16** (2021) (0) 2401086–2401086. ISSN 1880-6821. [10.1585/pfr.16.2401086](https://doi.org/10.1585/pfr.16.2401086).
- [21] K. A. Garcia, A. Bader, H. Frerichs, G. J. Hartwell, J. C. Schmitt, N. Allen, and O. Schmitz. Exploration of non-resonant divertor features on the Compact Toroidal Hybrid. *Nucl. Fusion*, **63** (2023) 126043. [10.1088/1741-4326/ad0160](https://doi.org/10.1088/1741-4326/ad0160).